Physics of the Earth and Planetary Interiors 279 (2018) 1–14

Contents lists available at ScienceDirect

Physics of the Earth and Planetary Interiors

journal homepage: www.elsevier.com/locate/pepi

Rupture process of the April 24, 2017, M_w 6.9 Valparaíso earthquake from the joint inversion of teleseismic body waves and near-field data

Javier A. Ruiz[a,*], Eduardo Contreras-Reyes[a], Francisco Ortega-Culaciati[a], Paula Manríquez[b]

[a] Departamento de Geofísica, Facultad de Ciencias Físicas y Matemáticas, Universidad de Chile, Santiago, Chile
[b] Centro Sismológico Nacional, Facultad de Ciencias Físicas y Matemáticas, Universidad de Chile, Santiago, Chile

ARTICLE INFO

Keywords:
Kinematic source inversion
Chile
Subduction zone
Earthquake source observations
Rupture process

ABSTRACT

The central Chilean margin (32°–33°S) is characterized by the subduction of the Juan Fernández Ridge (JFR) beneath the continental South American plate. The JFR corresponds to a hotspot track composed by seamounts typically 3–3.5 km high above the surrounding seafloor, with a ridge-trench collision zone underlying the prominent Valparaiso Forearc Basin (VFB). This region has been affected by several large and mega earthquakes, where the last event corresponds to a complex seismic sequence that took place at the southern edge of VFB in April 2017. The spatio/temporal distribution of the seismic events is characterized by a predominant southeast migration of the seismicity. An M_w 6.9 earthquake triggered two days after the sequence started and occurred at the northern end of the rupture area of the 1985 M_w 8.0 Valparaiso earthquake. We compute the kinematic rupture process of the 2017 M_w 6.9 Valparaiso earthquake from the joint inversion of teleseismic body waves and near-field data. The Akaike's Bayesian Information Criterion was used to objectively estimate both, the relative weighting between datasets and the weighting of spatial and temporal constraints used as a priori information. The coseismic slip is distributed over an area of dimensions $\sim 35 \times 10$ km^2, with a maximum slip of 1.5 m. The rupture propagated unilaterally downdip. The source duration from the moment-rate solution is ~ 20 s, with a total seismic moment of 3.05×10^{19} Nm (M_w 6.9). The analysis of the seismicity shows that most of the events occurred along the plate interface, foreshock clustered northern from the mainshock epicenter and the aftershocks occurred to the southeast, at a deeper location. The inverted regional moment tensors show similar faulting mechanism than the mainshock. The seismic sequence started two days before the mainshock and lasted for about two weeks, and a migration pattern of the seismicity was observed. The rupture of the 2017 M_w 6.9 earthquake nucleated where the San Antonio seamount (belonging to the JFR) is subducting, and propagated downwards along a zone that presents high interseismic coupling. The complex seismic sequence might be explained by an aseismic slip transient in the zone and the influence of the downdip migration of fluids from the accretionary prism along the subduction channel. The erosive and tunneling effect left by the sudden slip of the subducting seamount might provide the cavity for downdip migration of fluids and subsequent swarm seismicity.

1. Introduction

The Chilean convergent plate margin is frequently affected by destructive thrust earthquakes capable of generating devastating tsunamis (e.g. Nishenko, 1985; Comte and Pardo, 1991; Lomnitz, 2004). The seismic patterns observed during pre-, co-, and post-seismic periods are not yet well understood due to the complexity of the physics governing earthquake rupture. In April 2017, a moderate M_w 6.9 thrust earthquake took place offshore Valparaiso (Nealy et al., 2017; Ruiz et al., 2017), where the Nazca plate subducts beneath the South American plate at a current convergence rate of ~6.5 cm/yr in a N77°E direction (Khazaradze and Klotz, 2003). According to information published by the Centro Sismológico Nacional (CSN) of the Universidad de Chile, the origin time was April 24th, 2017, 21:38:28 (UTC time), with epicenter at 33.089°S, 72.116°W, and at 24 km depth. The moment magnitude computed by seismological agencies for this earthquake is M_w 6.9. Based on analyses of long-period waves and centroid moment tensor (CMT) solutions, the nodal planes estimated by the Global CMT Project (GCMT) are, 3°/16°/94° (strike/dip/rake) and 179°/74°/89°. The United States Geological Survey (USGS) W-phase CMT solution provides similar mechanism, 4°/14°/99° and 174°/76°/88°. Both agencies place the centroid depth at ~25 km. The causative fault is associated

* Corresponding author at: Blanco Encalada 2002, Santiago Centro, Santiago, Chile.
E-mail address: jruiz@dgf.uchile.cl (J.A. Ruiz).

https://doi.org/10.1016/j.pepi.2018.03.007
Received 19 January 2018; Received in revised form 27 March 2018; Accepted 28 March 2018
Available online 30 March 2018

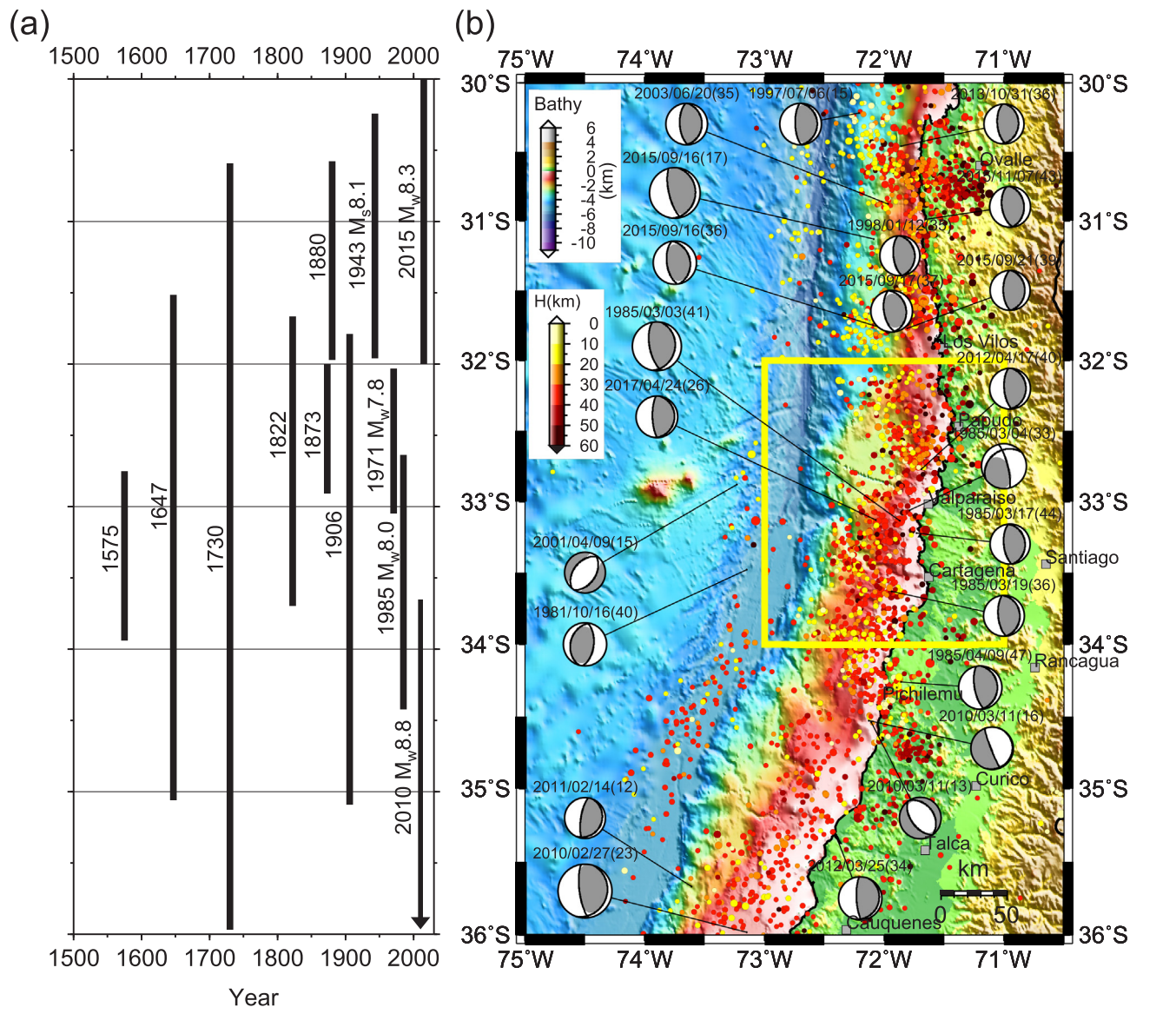

Fig. 1. (a) Space-time diagram of historical and instrumental large earthquakes occurred along central Chile. Thick black lines represent the estimated rupture lengths by Comte et al. (1986). For the 2010 M_w 8.8 Maule and 2015 M_w 8.3 Illapel earthquakes, the rupture lengths were taken from Moreno et al. (2012) and Lange et al. (2016), respectively, where the black arrow indicates the rupture extends beyond the rectangular area. (b) Map of the seismicity (colored circles) located by the NEIC ($M \geq 4.5$) between 01 March 1980 to 31 March 2017. We over imposed the centroid moment tensor solutions computed by the GCMT for events with $M \geq 6.5$, and above each beachball the date and centroid depth (in parentheses) are shown. The yellow rectangle depicts the study area. Colorbars for bathymetry and focal depth are also plotted. (For interpretation of the references to colour in this figure legend, the reader is referred to the web version of this article.)

with thrust faulting on a shallow plane dipping ~14°–16°, striking approximately north-south.

The hypocenter of the M_w 6.9 2017 Valparaiso earthquake is located about 30 km northwestward from the hypocenter of the latest large earthquake M_w 8.0 that occurred on March 3, 1985 offshore Valparaiso (Comte et al., 1986). The region of central Chile between 32°S and 35°S, has been shook by great earthquakes. For instance, a large earthquake occurred in 1575 (M ~7.0–7.5) near La Ligua (~32.27°S), and the largest ones occurred in 1647 (M ~8), 1730 (M ~8.5–9.0), 1822 (M ~8.0–8.5), and 1906 (M ~8.6), according to the historic records of Lomnitz (2004). In 1971, a thrust event M_s 7.5 triggered near La Ligua at 40 km depth (Malgrange et al., 1981), and in 1873, a similar event to the 1971, took place in the region between 32°S/33°S (Comte et al., 1986). Fig. 1a summarizes the estimated rupture lengths for the historical and instrumental earthquakes that have occurred in central Chile (Comte et al., 1986).

Fig. 1b shows an overall view of the seismicity located by the National Earthquake Information Center (NEIC) along central Chile since 1980 to 31 March 2017, with depths < 60 km and magnitudes larger than 4.5. The CMT solutions computed by the GCMT show that seismic events ($M \geq 6.5$) present a diverse variety of faulting mechanisms, but most of them have occurred in the plate interface. For instance, only two outer-rise events have been recorded since 1980, in 1981 and 2001. The 1981 event is related to an inverse fault, instead the 2001 was normal faulting.

In 2010, a M_w 8.8 megathrust earthquake shook south-central Chile with a total rupture length of ~500 km (e.g. Moreno et al., 2012), and was followed by a destructive tsunami. To the north, the rupture stopped at ~34°S, partially overlapping with the slip of the 1985 Valparaiso earthquake calculated by Mendoza et al. (1994). On September 16th, 2015, the M_w 8.3 Illapel earthquake broke from 32°S to 30°S, over a segment of 200 km length (e.g., Ruiz et al., 2016; Lange et al., 2016). Lange et al. (2016) analyzed the aftershock activity and observed several clusters of seismicity. In particular, further south of

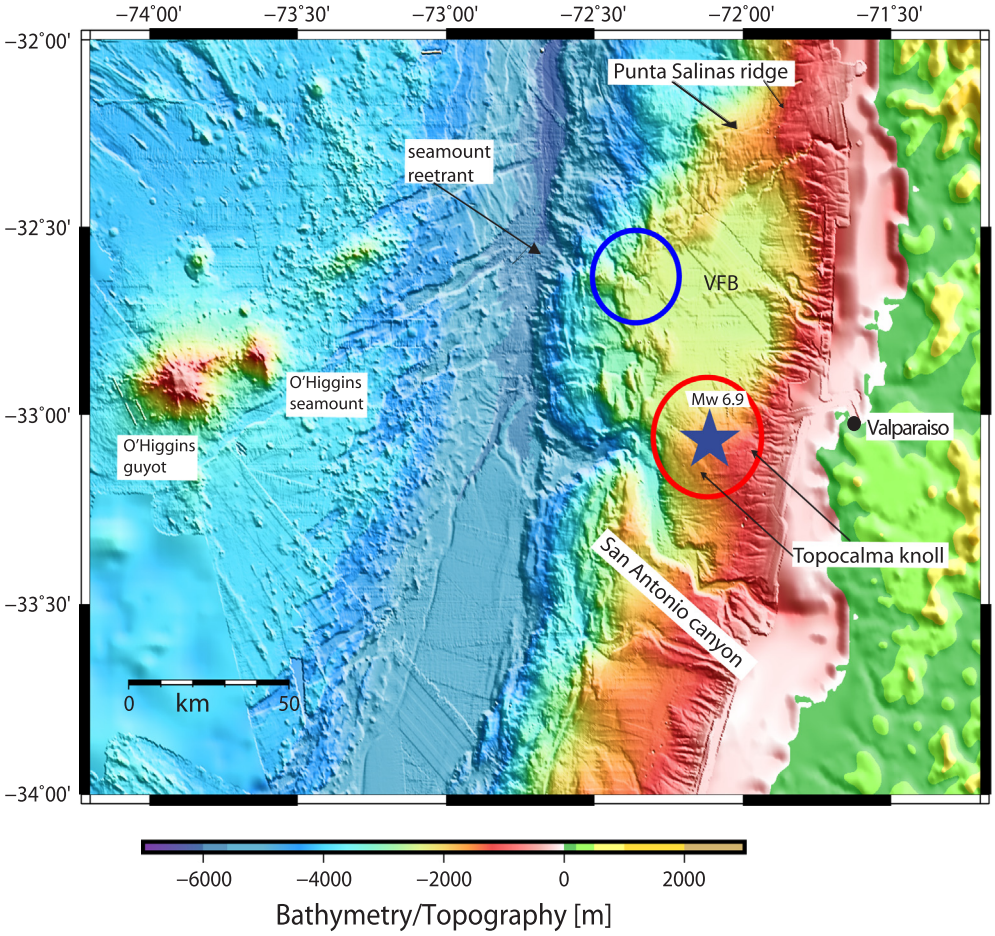

Fig. 2. (a) Swath bathymetric image of the seafloor off central Chile. The O'Higgins guyot and seamount correspond to the easternmost portion of the Juan Fernández Ridge before the collision with continental South American plate. Blue and red open circles denote the location of the subducted Papudo and San Antonio seamounts, respectively, according to the location of magnetic and gravimetric anomalies of Yáñez et al. (2001) and Flores (2007), respectively. The uplifted Punta Salinas Ridge is spatially coincident with the landward projection of the JFR. VFB: Valparaiso Forearc Basin. The uplifted Topocalma knoll spatially correlates with the subducted San Antonio seamount. The epicenter of the 2017 M_w 6.9 located by the CSN in shown by the blue star. (For interpretation of the references to colour in this figure legend, the reader is referred to the web version of this article.)

the southern limit of the Illapel rupture, near the Juan Fernandez Ridge, two distinguishable clusters appear. One of them is located at the Topocalma Knoll (~33°S; Fig. 2) which is likely related to the subduction of the San Antonio seamount, and a second one, located at ~33.3°S in the vicinity of the trench.

In April 2017, foreshock activity started and clustered near (72.1°W, 33°S) and a M 4.9 event was triggered in April 22. Afterwards, in April 24 the mainshock M_w 6.9 nucleated, and the seismic sequence lasted until the first week of May 2017. According to the NEIC earthquake catalog, three events with magnitudes ~6.0 were triggered in the region, a M 6.0 (April 23, 02:36 UTC), a M 5.9 (April 28, 15:30 UTC) and a M 5.8 (April 28, 16:05 UTC). After the mainshock event, seismicity clustered southeastward, near 33.3°S and 71.9°W. An overall space-time overview, indicates an apparent north to southeast migration of the reported seismicity.

Understanding the physics behind the rupture process of the M_w 6.9 Valparaiso earthquake allows getting an insight on the seismic cycle along a region affected by large earthquakes. The investigation and source characterization of well recorded earthquakes provide relevant information for seismic hazard evaluation along central Chile in the context of the occurrence of great earthquakes. It is also important to relate the complex seismic sequence in terms of the source characteristics of the mainshock.

The main goal of this study is to analyze the rupture process of the 24th April 2017 M_w 6.9, Valparaiso earthquake from the joint inversion of near-field and teleseismic datasets. We analyze the seismicity and we invert regional moment tensors for events ($M \geq 4$) associated to the seismic sequence that took place in April 2017 offshore Valparaiso. We investigate the whole seismic sequence and discuss its seismotectonic implications in terms of the geodynamic context of the study area.

2. Tectonic setting

The central Chilean margin is characterized by the collision of the Juan Fernández Ridge (JFR) with the trench at 32°–33°S (Fig. 2). The JFR is a hot spot track formed at the Juan Fernández Hotspot located some 900 km west of the Chile Trench (e.g. Laursen et al., 2002; Kopp et al., 2004). The easternmost, yet unsubducted portion of the JFR before subduction is composed by two prominent seamounts: the O'Higgins Guyot and seamount (~3500 m and ~3000 m above the surrounding seafloor, respectively; Fig. 2). The ridge-trench collision zone marks the transition from the poorly sedimented trench at the north to a sediment-flooded filled trench at the south. The collision zone is also characterized by the presence of the prominent Valparaiso Forearc Basin (VFB); a shelf basin with a 3.0–3.5 km thick sediment fill of late Cenozoic age (Laursen et al., 2002). The formation of the VFB has been attributed to the large subsidence rate of the margin caused by thinning of the continental crust due to the basal erosion processes enhanced by the JFR subduction (Laursen et al., 2002). Nevertheless, seismic refraction data provides evidence for an accretionary prism 30–40 km wide just seawards of the VFB (Flueh et al., 1998; Contreras-Reyes et al., 2015).

The landward flank of the VFB is highlighted by a spectacular trenchward dipping normal scarp interpreted as the superficial expression of a crustal discontinuity separating a subsided/collapsed marine forearc block from an uplifted coastal block belonging to the Coastal Cordillera (Contreras-Reyes et al., 2015). The northern and southern flanks of the VFB are shaped by two uplifted areas: the Punta Salinas Ridge and Topocalma knoll, respectively (Fig. 2). The uplifted surface along the Punta Salinas Ridge has been suggested to be caused by the subduction of the JFR (von Huene et al., 1997; Laursen et al.,

2002). The Topocalma knoll lies next to the San Antonio canyon (Fig. 2). Laursen et al. (2002) and Laursen and Normark (2002) proposed that the tectonic evolution of the Topocalma knoll is controlled by the subduction of the San Antonio seamount. These authors suggest that the collision of this seamount formed the San Antonio re-entrant and warped the middle slope along its landward advancing path (Fig. 2). The subduction of the San Antonio seamount has been evidenced by the analysis of gravimetric anomalies, and it is currently located at ~72°W/33°S (Fig. 2; Flores, 2007).

3. Data and methods

3.1. Seismological data

We select all the events (M ≥ 2.5) located by the CSN inside the rectangular region, 71°S–73°S and 32°W–34°W, with depths < 60 km, that occurred during April and May 2017. Based on this catalog, a subset of events (M ≥ 4.0) were chosen to compute the regional moment tensors, constrained using a database including all waveforms available at the NEIC and CSN. For each event, the three component waveforms were retrieved for broadband stations located at distances less than Δ ≤ 10° from the epicenter. To analyze the centroid moment tensor of the mainshock using the W-phase, we retrieved the LH channels of broadband stations of the Global Seismographic Network (GSN) with epicentral distances up to 30°.

In the finite-source inversion, teleseismic body waves and strong motion datasets are used. Teleseismic broadband data were available through the Data Management Center of the Incorporated Research Institutions for Seismology (IRIS-DMC). We selected three components broadband waveforms from stations located between 30° to 90° distance from the epicenter and with a good azimuthal coverage around the source. We also use acceleration records (three components) of strong motion stations located in the near-field and regional distances (Δ ≤ 300 km) that were downloaded from online facilities maintained by the CSN (http://evtdb.csn.uchile.cl/). To complement strong motion data, we included non-saturated records from five broadband stations.

3.2. Moment tensors

3.2.1. W-phase inversion

We applied the W-phase moment tensor inversion (Kanamori and Rivera 2008) to compute the long-period source characteristics of the mainshock. This algorithm estimates the centroid moment tensor from the W-phase, which is a long-period phase observed on broadband seismic records (100 s–1000 s) between the P and S waves (Kanamori, 1993). This method has been broadly used in real-time operations using teleseismic broadband data and it has been extended successfully to low magnitude earthquakes M_w ~5.8 (Hayes et al., 2009). Duputel et al. (2011) demonstrated the robustness of the algorithm applied at regional distances.

In this study, we use the W-phase algorithm implemented by Duputel et al. (2012) and available through the web site, http://wphase.unistra.fr that incorporates a Green's function database computed for epicentral distances, Δ, up to 30° for regional applications. The extension of the method to regional data needs to enlarge the W-phase time window at short distances and the following time window is used,

$$t_w = \begin{cases} [t_p; t_p + 15 \times 12^\circ] & \Delta \leqslant 12^\circ \\ [t_p; t_p + 15 \times \Delta] & \Delta \geqslant 12^\circ \end{cases} \quad (1)$$

which was the one used by Roch et al. (2016), where t_P represents the P-wave arrival time. The frequency band was set according to the band-pass filter magnitude-dependent suggested in the same study. A time domain deconvolution method is used to extract the W-phase from the broadband records and a 4th order Butterworth bandpass filter is applied to synthetics and observed waveforms. A grid-search scheme is used to estimate the best centroid location (longitude, latitude and depth), time-shift and half-duration.

3.2.2. Regional moment tensor

We compute regional moment tensors from broadband records using the Time-Domain Moment Tensor (TDMT) inversion code (e.g. Pasyanos et al., 1996; Dreger, 2003). This software is routinely used in earthquake monitoring. The TDMT inverts the deviatoric seismic moment tensor in the time-domain by solving a linear inverse problem in the least square sense. The processing of broadband waveforms includes removing the instrument response, rotation to the great-circle path, and its integration to obtain ground displacements. A causal 4th pole Butterworth bandpass filter is applied to synthetic and observed seismograms prior to run the inversion. The optimal frequency band depends on the magnitude of the earthquake and we used the frequency cut-offs as suggested by Kubo et al. (2002).

The hypocenter location is needed as input, and then, at the assumed epicenter location, we search the best centroid depth in a 2 km spaced grid over a depth range, and select the solution that yields the largest variance reduction (VR), or minimum RMS (root mean square). The VR is the goodness-of-fit parameter between the data and synthetics and a variance reduction of 100% would indicate an exact match between the observed and synthetic waveforms (e.g. Pasyanos et al., 1996).

The deviatoric moment tensor is decomposed in standard form to obtain the double-couple (DC) and a compensated linear vector dipole (CLVD) moment tensor. The synthetic Green's functions are computed for a 1D velocity crustal model using the frequency-wavenumber integration method proposed by Saikia (1994). The velocity crustal model used in our study was the one used by the CSN in central Chile (Massone, personal communication, 2017).

3.3. Finite fault inversion

3.3.1. Inverse method and source model

The inverse method used in this study follows the approach by Ide and Takeo (1997). The kinematic inversion approach relies on a discrete fault system to represent the spatial distribution of the slip, but uses a more general representation than conventional methods. Basically, the slip-rate is expanded as a linear combination of 2D spatial and temporal basis functions, where the expansion coefficients are unknown model parameters. Each basis function along-strike, -dip and -time directions is defined as a linear B-spline. Thus, slip is continuous everywhere spatially and temporally.

Using the representation theorem of seismic sources, the equation that relates observed and synthetic displacements written in vector form is (e.g. Ide and Takeo, 1997),

$$\mathbf{d} = \mathbf{Gm} + \mathbf{e} \quad (2)$$

where **d**, **m**, and **e**, are the data, parameter and error vectors of the problem, respectively. **G** is an *N* (number of data), times *M* (number of parameters), matrix representing the Green's function of the problem. The error vector contains measurements and modeling errors, and for simplicity one can assume that errors follow a Gaussian distribution.

Two types of smoothing constraints, temporal and spatial, are used as a priori information introduced to maintain stability during the inversion. The temporal constraint is the finite difference operator of first-order partial derivative of slip-rate by time. Instead, the spatial constraint corresponds to the Laplacian finite difference operator applied to the total (static) slip. The weighting factors of the smoothing constraints are determined by minimizing the Akaike's Bayesian Information Criterion (ABIC), which is formulated on the principle of maximizing entropy (Akaike, 1980). The non-negative least squares (NNLS) method of Lawson and Hanson (1974) is used to solve the damped least square problem, to ensure positivity of the model

parameters which mean, parameters are equal or larger than zero. Refer to Ide and Takeo (1997) for further details.

3.3.2. Data processing and fault model parameterization

We use records from 24 strong motion and 5 broadband stations located up to 300 km from the epicenter, with sampling rates of 100 Hz and 40 Hz respectively. A map with the distribution of all near-field stations is shown in Fig. S2. The acceleration records were integrated twice to obtain ground displacements, filtered in the band of 0.02–0.40 Hz (50 s–2.5 s) and resampled to a time-step of 0.25 s. For broadband stations, the instrument response was removed from broadband waveforms, integrated once to obtain displacements, and filtered in the same frequency band as strong motion data.

The processing of teleseismic waveforms includes, deconvolution of the instrument response, integration to obtain ground displacement, and windowing 60 s around the body wave arrivals, starting 10 s before the respective P- or SH-wave arrival time. We select 78 P-waves (vertical) and 40 SH-waves (horizontal transverse). Teleseismic data were bandpass filtered between 0.005 and 1 Hz (200 s–1 s) and resampled to 0.25 s.

The fault geometry was built based on the focal mechanism retrieved in this study (via the W-phase) and moment tensor solutions published by USGS and GCMT (see Table 1 for more solutions). Slab 1.0 (Hayes et al., 2012) is used as reference for the plate interface and to account for variations of the geometry along dip. Preliminary inversion test were run before setting the final source model parameterization, using a criterion based on the stability and size of the estimated model. The final assumed rectangular fault ($L \times W = 76.5 \times 76.5\,km^2$) was divided into four rectangular segments along dip, the first three set at 20 km width each and the last one 16.5 km width, dipping with 12°, 14°, 16°, and 18°, from top to bottom, respectively. Fig. S3 shows the final fault geometry compared against Slab 1.0. The strike was fixed at N0°E. We use the hypocenter located by the CSN, but the source depth was shifted to 17 km which is consistent with the Slab 1.0 geometry. We use a total of 16, 16 and 11 basis functions along-strike, -dip, and -time directions, respectively, to represent the slip in one direction. The spacing between knots of the linear B-splines in the 2D spatial domain was set at 4.5 km in both, strike and dip, directions. The 11 basis functions in the time direction, have 2 s duration each and 50% of overlapping. Therefore, the maximum rise-time allowed is 12 s. The total slip at each grid point is allowed to vary with a rake between 90° ± 45°. The maximum rupture velocity was fixed at 90% of the shear-wave velocity in the vicinity of the hypocenter depth. This value controls the propagation of a rupture front that expands radially from the hypocenter and controls the onset rupture time of the first knot of the slip-rate for each point on the fault when the rupture front reaches it. A slower rupture velocity than the maximum value is allowed and it is achieved by a proper choice of the expansion coefficients.

The 1D regional crustal velocity model used by the CSN along central Chile (Massone, personal communication, 2017) was set to compute near-field waveforms and teleseismic body waves. The synthetic near-field Green's functions were computed in a horizontally stratified medium using the numerical code AXITRA (Coutant, 1989) based on the discrete wavenumber method of Bouchon (1981). Teleseismic body waves Green's functions were computed using the approach of Kikuchi and Kanamori (1991). We use a time-step of 0.25 s to compute all synthetic Green's functions and were filtered in the same frequency band as the respective observed waveforms.

3.3.3. Joint inversion methodology

In order to invert near-field and teleseismic body waves in a jointly manner, we applied the method developed by Funning et al. (2014) that treats simultaneously the problem of objectively estimating the relative weighting between datasets, as well as the temporal and spatial smoothing constraints. The authors derive the ABIC for the joint inversion of multiple datasets and show the feasibility of the method by inverting InSAR and teleseismic data for the 1997 M_w 7.6 Manyi, Tibet, earthquake.

In our study, we use the method of Funning et al. (2014) to invert near-field and teleseismic body waves data jointly, but we keep the source model parameterization and smoothing constraints proposed by Ide and Takeo (1997). In the supplementary material, we briefly present the methodology and results for the estimation of hyperparameters, damping parameters and relative variances of datasets, based in the ABIC criterion.

4. Results

4.1. W-phase of the mainshock

We applied the W-phase inversion in the frequency band 0.002–0.01 Hz (500 s–100 s) to compute the seismic moment tensor of the mainshock using regional ($\Delta \leq 30°$) broadband records. The best-fitting regional moment tensor (Fig. S1) yields inverse faulting solution with nodal planes of 356°/15°/88° and 177°/75°/91°. The best centroid location is estimated at (71.997°W, 33.189°S) and 19.5 km depth. The half duration of this event is 9 s, a seismic moment of 2.43×10^{19} Nm and with a moment magnitude of 6.86. The azimuthal gap of our solution is 154° and a total of 54 channels were used. Our solution is rather similar to the ones obtained by NEIC or GCMT, showing a fault plane striking north-south with a low dipping angle. Table 1 summarizes earthquake source parameters determined by GCMT, USGS, GEOFON, GEOSCOPE and this study. All the solutions present similar moment magnitude, $M_w \sim 6.9$. Centroid source depth varies from 19 to 26 km. A large scatter is observed for the half duration, which can be attributable to methodological differences in the resolution of the inverse problem, in the frequency bands used to filter waveforms, or the seismic waves being inverted (e.g., surface waves, W-phase).

4.2. Seismicity

The overall space-time evolution of the seismicity ($M \geq 2.5$) located by the CSN between April 1st to May 7th, 2017, is shown in Fig. 3. The analysis of the frequency of events over time show that for about two weeks over 3–4 events per hour, were recorded, reaching a peak of ~17 (Fig. 3a). The seismicity rate increased abruptly in April 22 and decreased during the first week of May 2017 (Fig. 3b).

The spatio-temporal distribution of the seismic events (Fig. 3c, d

Table 1
Earthquake source parameters and focal mechanisms of the 24 April 2017 M_w 6.9 Valparaiso earthquake computed by different seismological agencies and this study. The centroid location is given by longitude (Lon), latitude (Lat), source depth (Depth) and half-duration (Hd). NP1 and NP2 are nodal planes (strike/dip/rake), scalar seismic moment (M_0) and moment magnitude (M_w).

Agency	Lon [°]	Lat [°]	Depth [km]	Hd [s]	NP1	NP2	M_0 [N.m]	M_w
GCMT	−72.07	−33.13	26	6.1	3/16/94	179/74/89	2.42×10^{19}	6.9
USGS	−72.062	−33.038	25.5	15	4/14/99	174/76/88	2.77×10^{19}	6.9
GEOFON	−71.89	−33.02	22	–	3/17/95	178/73/88	1.9×10^{19}	6.8
GEOSCOPE	−72.042	−33.056	19	–	0/19/95	176/71/88	3.21×10^{19}	6.94
This study	−71.997	−33.189	19.5	9	356/15/89	177/75/90	2.43×10^{19}	6.86

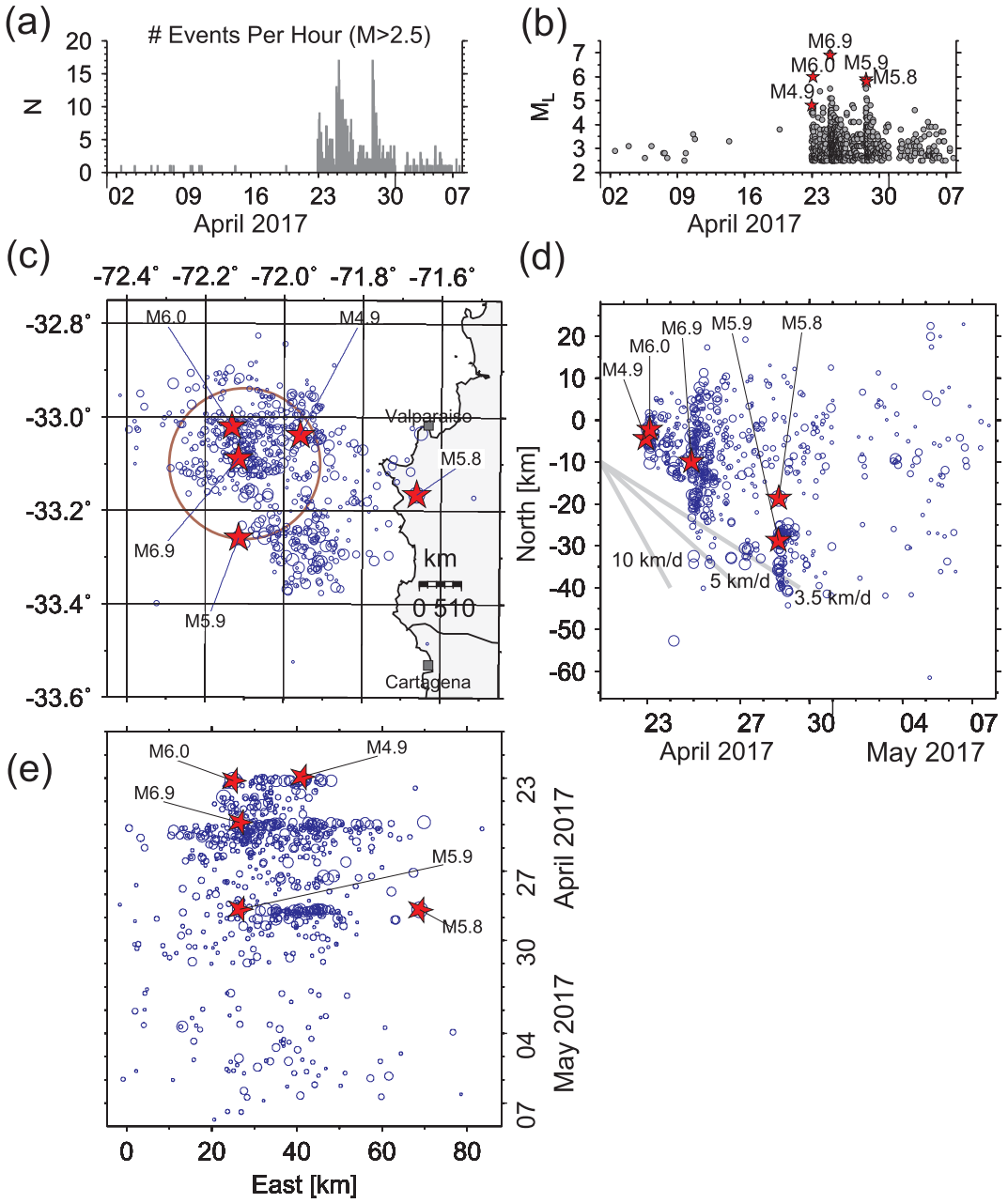

Fig. 3. Space-time representation of the seismic sequence of April 2017 located by the CSN between 1st April and 7th May, with depths < 50 km. (a) Seismicity rate, represented as the number of events per hour as function of time and (b) time series of event magnitude versus time. (c) Map with the spatial distribution of seismicity depicted by blue circles scaled with magnitude and the largest events highlighted by red stars. Temporal evolution of the seismicity represented as a function of the (d) northing and (e) easting coordinates. In panel (c, d, and e) the seismicity is plotted from April 21 to May 07. The brown circle represents the base of the San Antonio seamount off shore Valparaiso. (For interpretation of the references to colour in this figure legend, the reader is referred to the web version of this article.)

and e) strongly suggest that the seismicity migrated mainly from the north to the southeast, with an apparent propagation speed fluctuating between 3.5 and 5 km/day and estimated southward (Fig. 3d). After the mainshock occurred, seismicity clustered to the southeast, near (71.9°S, 33.3°S).

4.3. Regional moment tensors

Fig. 4 shows a total of 90 events with their respective regional moment tensor solutions computed using the TDMT software. Table S1 present all our solutions, where we kept those with VR larger than 40% and obtained with at least 3 stations. All the events analyzed present inverse faulting mechanism, with strike oriented mainly north-south, and with similar focal mechanism as the mainshock. Two clusters of events are observed (Fig. 4a). Events located northward from the epicenter of the mainshock spread over a circular region of 25 km radii, and occurred at shallower depths compared to the second cluster located southeastward. The events associated to the southern cluster broke a deeper seismogenic zone of the megathrust and spread over a much more compact region compared to the northern events. Fig. 4b and c show that the best centroid depth of the events analyzed correlates well with the plate interface given by Slab 1.0 (Hayes et al., 2012). Moment tensor solutions delineate well the width of the seismogenic zone affected along each profile. The regional moment tensor analysis done by other groups show overall similar characteristics and solutions (Ruiz et al., 2017; Nealy et al., 2017) as the ones presented in this study. Particularly, most of the events are consistent with thrust faulting occurring along the plate interface.

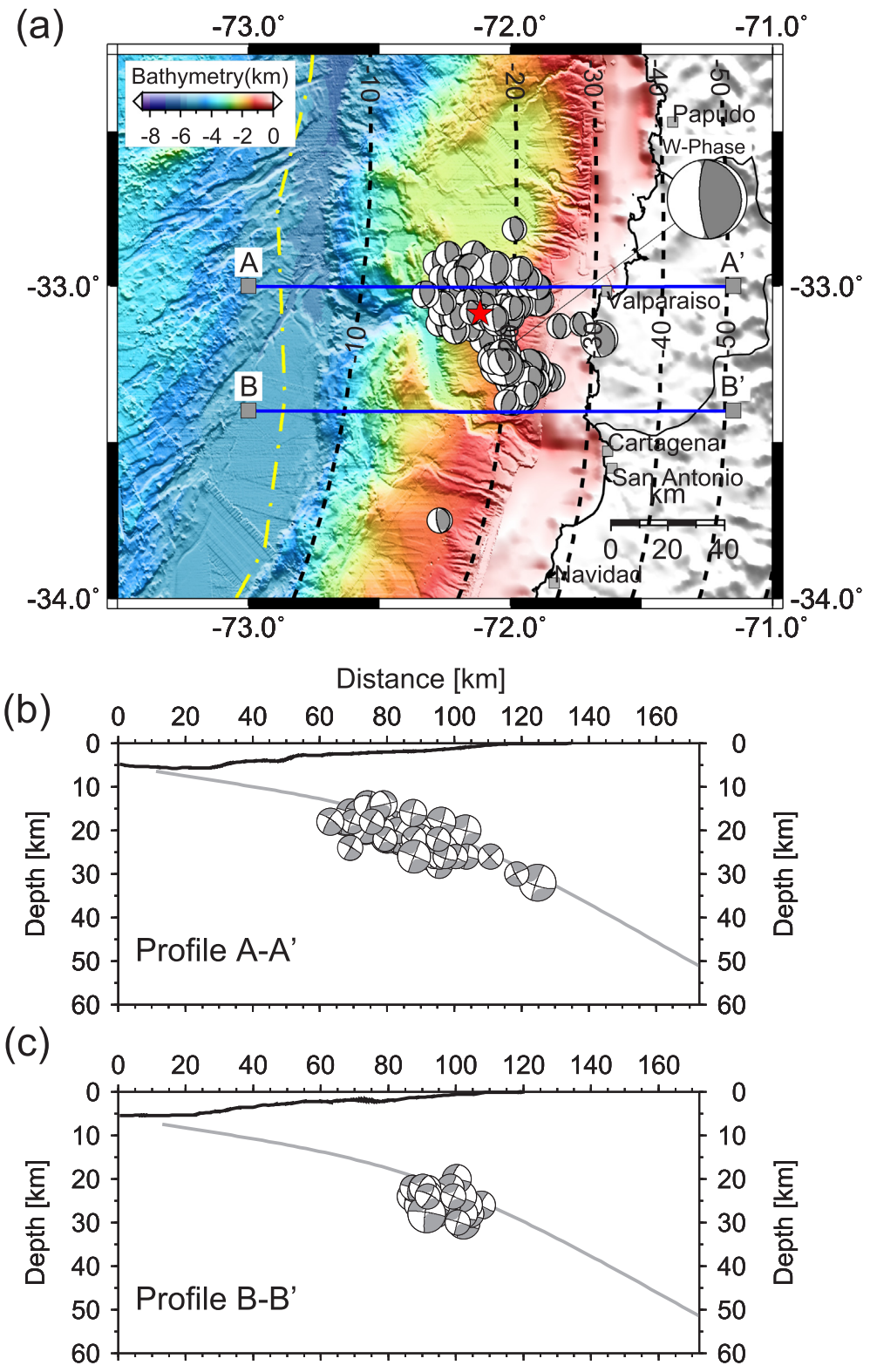

Fig. 4. Regional moment tensor solutions for events M ≥ 4.0 (depth < 60 km) that occurred between 01 April and 31 May 2017 in the study area. (a) Map with the spatial distribution of moment tensors and the W-phase CMT solution computed in this study. Red star is the epicenter of the April 24 2017 Valparaiso earthquake located by the CSN. Yellow dot-dashed line is the trench axis and dashed black lines are the isodepth contours of the plate interface (Slab 1.0 model, Hayes et al. (2012)). (b) and (c) are two cross-sections (A-A′ and B-B′, respectively) showing the distribution of the centroid depths and back projected focal mechanisms along each profile. Black line is the ocean bottom and gray line is Slab 1.0 (Hayes et al., 2012).

The northern cluster occurred before the mainshock, and the southern cluster occurred after it. The largest magnitude of the sequence was an M_w 6.0 that occurred in April 23, at 02:30 (UTC), the day before the M_w 6.9 earthquake occurred. The W-phase centroid location computed in this work is located approximately in the middle of the two clusters. Hence, foreshocks and aftershocks surround the W-phase CMT centroid location.

4.4. Finite source rupture process of the mainshock

We applied the joint inversion method detailed in the supplementary material that is based on the work of Funning et al. (2014). The relative weighting between datasets and the smoothing constraints are determined minimizing the ABIC. Fig. S4 shows the ABIC distribution and the optimal set of hyper-parameters obtained after a 3D grid search over the hyper-parameter space. The minimum ABIC was found at

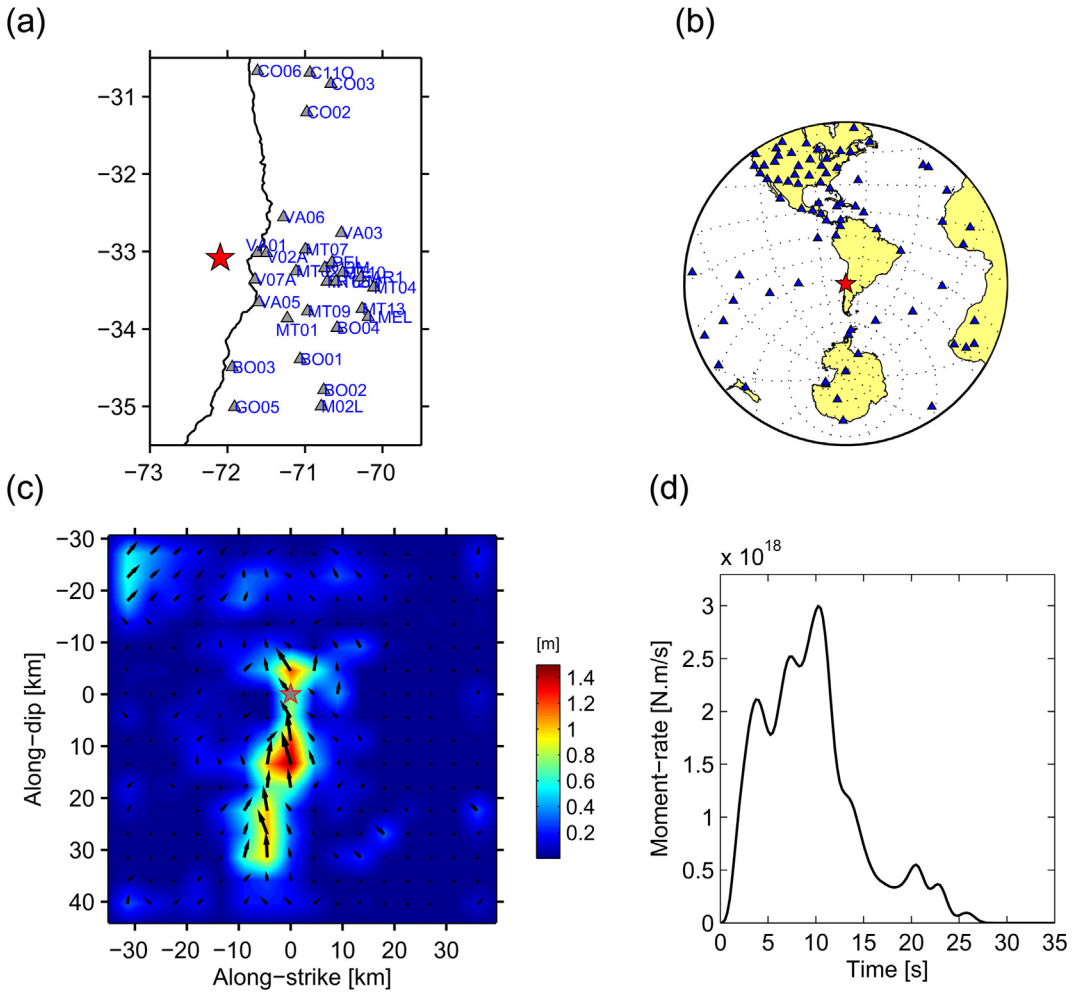

Fig. 5. Coseismic slip model for the 2017 M_w 6.9 Valparaiso earthquake obtained from the joint inversion of near-field and teleseismic body waves data. (a) Map with the location of strong motion and broadband stations used in the inversion. Red star is the epicenter located by the CSN. (b) Global distribution of teleseismic broadband stations (blue triangles) and the epicenter location (red star). (c) Final slip distribution. Black arrows represent the slip vector scaled to the total slip amplitude and gray star indicates the rupture nucleation point. Colorbar represents the slip amplitude in m. (d) Moment-rate function. (For interpretation of the references to colour in this figure legend, the reader is referred to the web version of this article.)

$\alpha = 1.06 \times 10^{-3}$, and $\beta = 1.13 \times 10^{-2}$, for spatial and temporal smoothing constraints, respectively. Instead, the optimal value of the hyperparameter controlling the relative weighing between datasets was found at $\gamma = 113.7$.

Fig. 5 summarizes the final slip model obtained from the joint inversion of teleseismic body waves and near-field data. Fig. 5a shows a map with the stations used in the near-field and the distribution of teleseismic stations at global scale is shown in Fig. 5b. The slip distribution is characterized by a narrow and elongated shape of dimensions $35 \times 10\,km^2$ with the largest dimension extended downdip from the hypocenter (Fig. 5c). Our solution shows a rupture front propagating mainly unilaterally downward, but also with a broken zone upward from the hypocenter. The peak-slip is about 1.5 m and is located at 15 km distance along dip from the rupture nucleation point. The total seismic moment is 3.05×10^{19} Nm and gives a moment magnitude of 6.9, which is in the same order as the one obtained by the W-phase inversion (see Table 1). From the solution, most of the moment occurs over the first 20 s (Fig. 5d). The maximum moment-rate occurs at 10 s after the rupture nucleation and reaches a peak value of 3.0×10^{18} Nm/s. From the final slip solution, one can observe three subevents associated with three patches of slip, one located around the hypocenter, the largest one occurring at 15 km from the hypocenter, and the last one at 25 km, measured downwards along-dip.

Fig. 6 shows the fit between observed and synthetic waveforms for the two datasets. The near-field synthetic ground displacements adjust very well the observed ones, in terms of both, waveforms and amplitudes (Fig. 6a). The misfit for this dataset gives a VR = 90%. Similarly, Fig. 6b shows a comparison between observed and synthetic teleseismic waveforms (P- and SH-waves). There is good agreement between observed and synthetics when comparing amplitudes, polarities, and waveforms. The VR computed for teleseismic body waves is 77%. The north component of the B004 station presents a long period component, thus this channel was not taken into account in the inversion.

The spatio-temporal evolution of slip-rate is shown in Fig. 7. The maximum rupture speed set in the inversion is $V_r = 3.6$ km/s. The rupture expands circularly during the first 5 s and then continues with unilateral downwards propagation. The rupture speed from the solution reaches the maximum value set in the inversion and the maximum slip-rate is about 1 m/s.

5. Discussion

Fig. 8a summarizes the space-time distribution of the seismic sequence of April 2017 and the coseismic slip model estimated in this study. We highlighted only events ($M \geq 2.5$) located by the CSN that occurred between April 22 to May 07 and the distribution at depth is shown in Fig. 8b. An intense foreshock activity, that lasted for two days approximately, preceded the rupture of the 2017 M_w 6.9 earthquake.

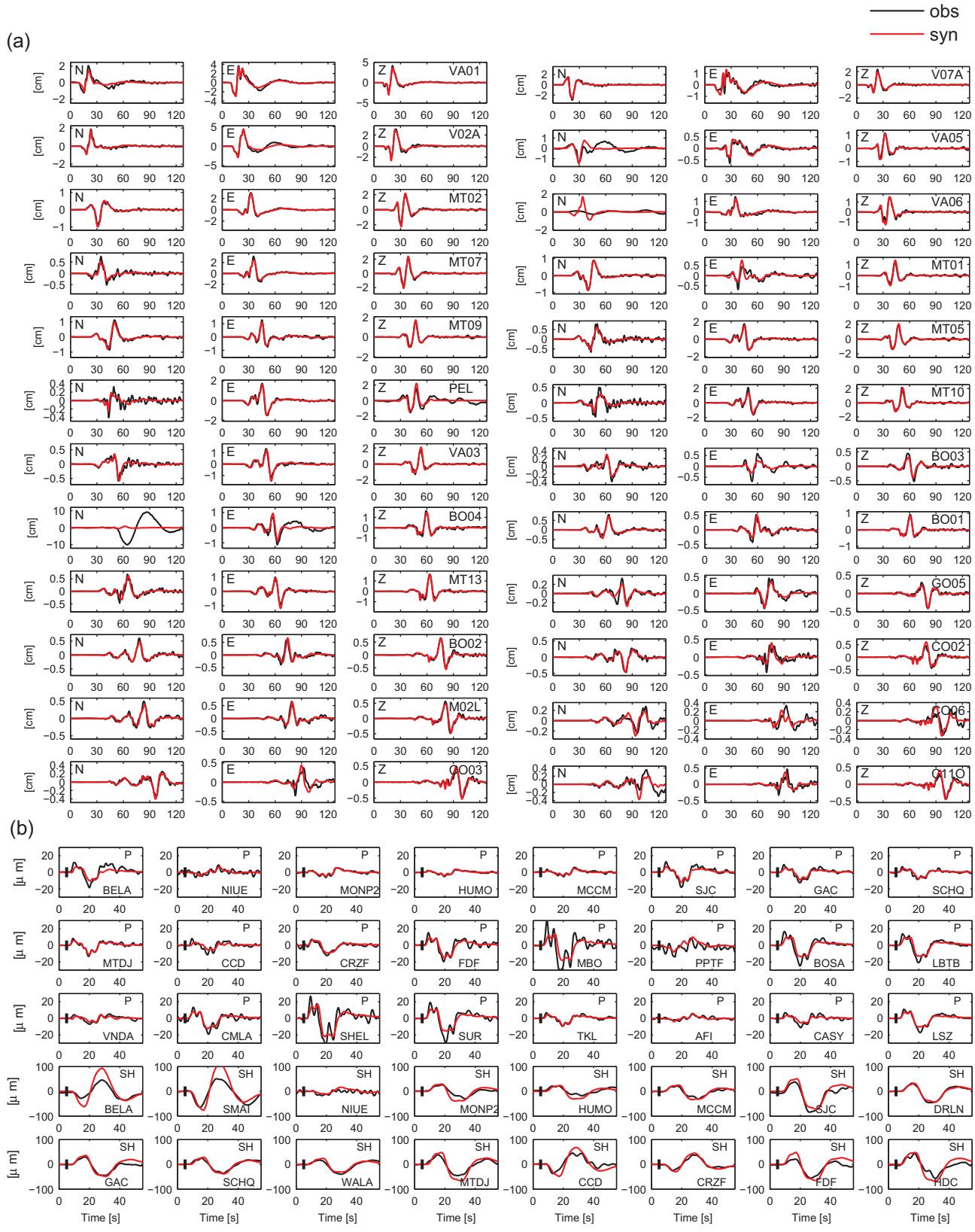

Fig. 6. Comparison of the observed (black line) and synthetic (red line) ground displacements. (a) Waveforms fitting for strong motion and broadband stations used in the near-field. The station name and components are indicated at the top of each trace. Start time of the records corresponds to the origin time of the event determined by the CSN. (b) Waveforms fitting for teleseismic body waves at several representative stations. Station name and the corresponding P- or SH-wave record is shown inside each box. (For interpretation of the references to colour in this figure legend, the reader is referred to the web version of this article.)

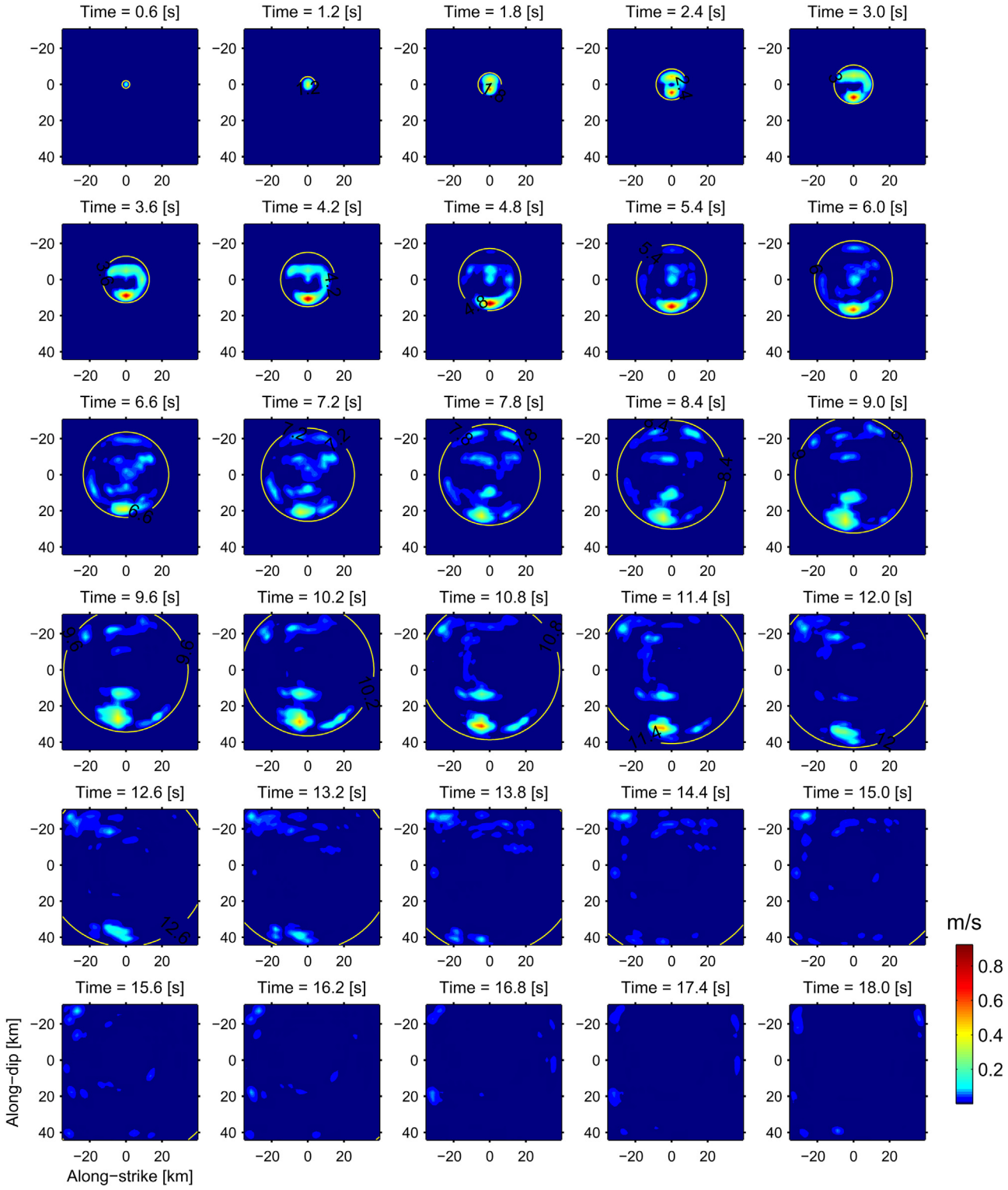

Fig. 7. Snapshots of the slip-rate plotted every 0.6 s after the rupture initiation (elapsed time is indicated at the top of each fault plane). Yellow contours correspond to the rupture front that propagates at the faster rupture speed set in the inversion which is, Vr = 3.6 km/s. Colorbar indicates the slip-rate amplitude in m/s. (For interpretation of the references to colour in this figure legend, the reader is referred to the web version of this article.)

The mainshock nucleated on April 24 and the rupture propagated circularly in a first stage and then unilaterally downward along dip. Aftershocks followed for three days until an M_w 5.9 event broke the plate interface 20 km southward from the epicenter of the mainshock. Then, a second seismic sequence was triggered and continued a few days, clustering southeastward from the epicenter of the mainshock. The slip of the M_w 6.9 event is spatially heterogeneous and extended for about 35 km long, occurring over a narrow slip band, reaching a peak-slip of 1.5 m that took place at 21 km depth. The slip model of Nealy et al. (2017) shows large slip (with a peak of ~1 m) along the downdip section of the megathrust and to the southeast of their assumed hypocenter. The slip model of Ruiz et al. (2017), based on a dynamic

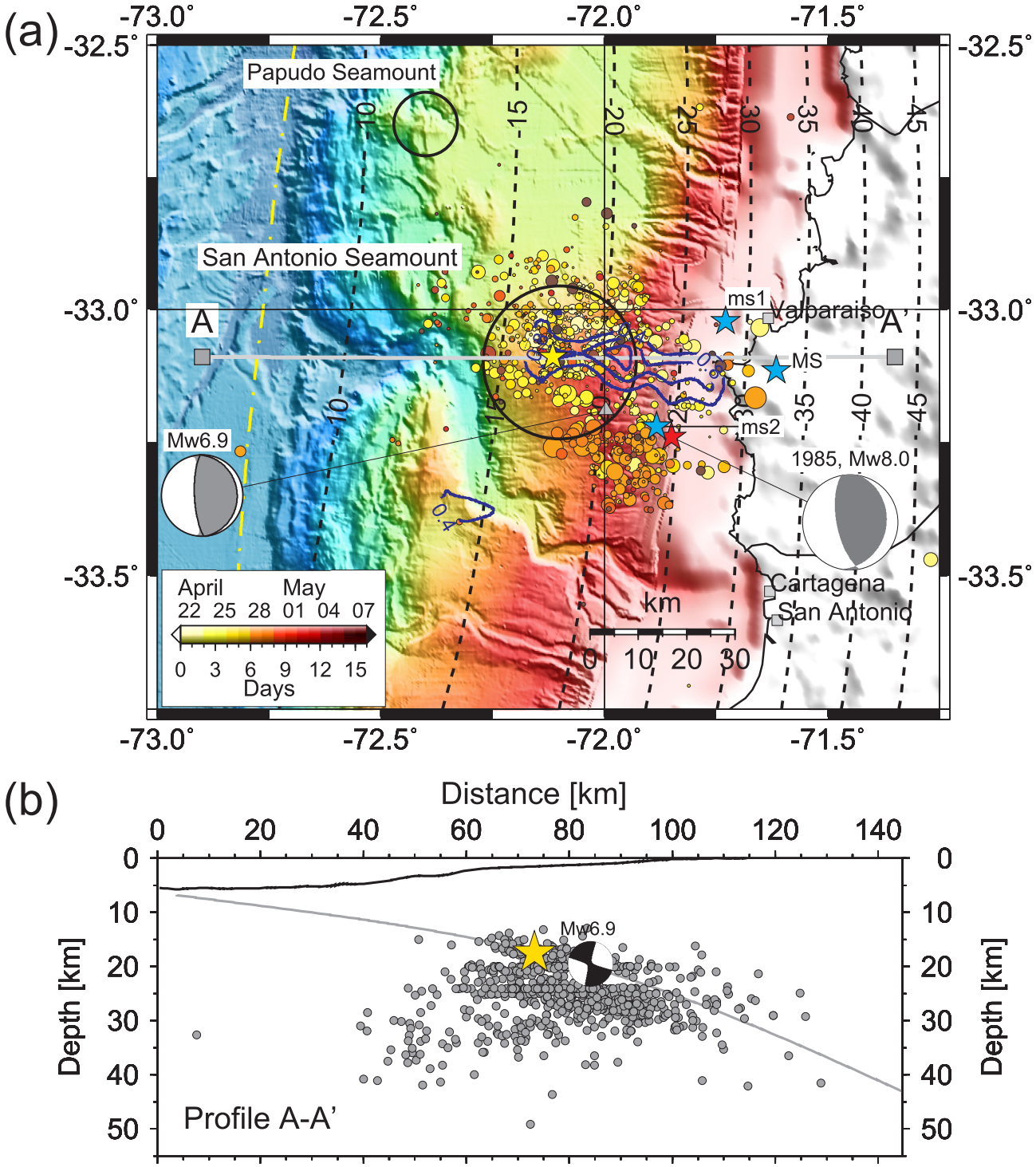

Fig. 8. (a) High resolution bathymetric map (Contreras-Reyes et al., 2015) and the space-time evolution of the seismicity located by the CSN (M ≥ 2.5) between 22 April to 07 May 2017. Colored circles represent the epicenter of events, with their sizes scaled to the magnitude and colorscale is the elapsed time in days since 22 April 2017 (UTC). Beach balls represent the W-phase CMT solution for the April 24 2017 M_w 6.9 Valparaiso earthquake (this study) and the focal mechanism of the March 3 1985 M_w 8.0 Valparaiso earthquake (Comte et al., 1986). The yellow, red, and cyan stars represent the epicenter of the 2017 M_w 6.9 event located by the CSN, the epicenter of 1985 M_w 8.0 earthquake (Comte et al., 1986), and the three energy burst (ms1, ms2, and MS) of the 1985 M_w 8.0 earthquake (Choy and Dewey, 1988), respectively. Open black circles are the Papudo and San Antonio seamounts. The slip distribution of the 2017 M_w 6.9 event is represented by the blue lines that correspond to 0.4 m slip contours. Dot-dashed yellow line is the trench axis. Dashed black line is the Slab 1.0 model (Hayes et al., 2012). (b) Distribution of hypocenter depths of the seismic sequence along the cross-section A-A′. The beach ball and the yellow star are the moment tensor solution and the assumed hypocenter depth used in the inversion of the M_w 6.9 event, respectively. Dark line is the ocean bottom and the gray line is the plate interface (Slab 1.0, Hayes et al., 2012). (For interpretation of the references to colour in this figure legend, the reader is referred to the web version of this article.)

inversion using strong motion records, presents an elliptical patch of semi-axis 10 km and 5 km, with a peak-slip of 2.7 m, that occurred within a much more compact zone than Nealy et al. (2017) solution and the one presented in this study. These differences arise, for instance, because of the different source inversion methodologies used, datasets, frequency band applied.

The interseismic coupling model available for central Chile obtained assuming a back-slip model, reveals four segments that present high coupling and are delimited by narrow areas of low coupling (Métois et al., 2012). In the study area, the average coupling coefficient versus latitude computed by Métois et al. (2012) shows a peak of higher coupling at ~32.9°S comparative to the values estimated for the whole Metropolitan segment, spanning from 33.5°S to 30°S. The authors interpret it as a small asperity that may have ruptured during the 1985 M_w 8.0 Valparaiso earthquake. The peak is located nearby where the seismic sequence of April 2017 started. The seismic sequence occurred approximately at the northern end of the rupture area of the 3 March 1985 M_w 8.0 Valparaiso earthquake (Mendoza et al., 1994). From a wide-band data analysis of the 1985 earthquake, the slip model of Mendoza et al. (1994) covers an area of about 200 km length, with the largest slip area centered near 33°S. Choy and Dewey (1988), identified two precursory phases separated 11 s in time (labeled as ms1 and ms2) in the data of the 1985 M_w 8.0 earthquake. The ms1 and ms2 phases occurred 17 s prior to the mainshock onset (labeled as MS), and were considered by the authors as part of the whole rupture process. The epicenter of each of these three shocks are labeled in Fig. 8a. The epicenter of the 1985 earthquake determined from the central Chile network data by Comte et al. (1986) is located 30 km southeast from the 2017 M_w 6.9 event (Fig. 8a). Somehow similarly to the 2017 M_w 6.9 earthquake, the 1985 M_w 8.0 mainshock was also preceded by 11 days of intense foreshock activity (Comte et al., 1986), thus suggesting that the entire sequence of April 2017 is part of a complex rupture nucleation, leading to trigger the mainshock.

We observe a migration of the seismicity that started north (at ~33°S) from the epicenter of the mainshock and migrated to the southeast at an apparent velocity of ~3.5 km/day estimated southward. Most of the seismic events occurred off the broken area by the mainshock. The migration of seismicity may be associated with an aseismic slip transient in the zone, where the propagation of slow-slip through the plate interface leads to trigger the mainshock. A somehow similar seismicity pattern, at different space-time scales, was observed in the case the 2011 M_w 9.0 Tohoku-Oki (e.g. Kato et al., 2012) and 2014 M_w 8.1 Pisagua (e.g. Ruiz et al., 2014; Kato et al., 2016) earthquakes. In both cases, a slow slip event occurred in the rupture area prior to the mainshock and a clear migration of seismicity was observed. For instance, Ruiz et al. (2017) analyzing cGPS (continuous Global Positioning System) time series suggested that a slow slip event preceded and triggered the M_w 6.9 earthquake. Further analysis of this hypothesis is out of the scope of this study.

Major bathymetric features (e.g. seamounts, ridges, fracture zones) along subduction zones have been proposed to induce heterogeneities and spatial variations in mechanical and frictional properties on the megathrust when subducted (e.g., Contreras-Reyes and Carrizo, 2011). The subduction of these major oceanic features can act as either asperities or barriers for earthquake rupture propagation, while also increasing the hetereogeneity of seismic coupling between the overriding and subducting plates. For instance, subducting seamounts may increase the normal stress between the subducting and overriding plates, and increase the interplate coupling (Scholz and Small, 1997). On the other hand, seamounts or similar high oceanic features are presumed to act as barriers, where the earthquake rupture stops or slowdowns (e.g. Kodaira et al., 2000).

Mochizuki et al. (2008) conducted an active-source seismic survey with ocean bottom seismometers monitoring, which has revealed the subduction of a large seamount near a region of repeating earthquakes of magnitude M ~7 in the southern Japan Trench megathrust. From the analysis of long-term seismicity, the authors found a sequence of repeaters M ~7 that have broken an area of the megathrust next to – and not over – the seamount with an interval of ~20 yr. Based on the absence of seismicity over the seamount and because the rupture of 1982 M_w 7.0 event started at the base of the seamount and propagated downward, Mochizuki et al. (2008) proposed very weak interplate coupling over the seamount. Thus, the aseismic behavior at the plate interface on top of the seamount may be common on sediment rich subduction zones. However, high coupling on top of the seamount can be possible (Mochizuki et al., 2008).

It has been largely debated and nowadays it is not absolutely well understood, if subducted seamounts trigger earthquakes, or act as barriers by slowing down or arresting rupture propagation (e.g. Scholz and Small, 1997; Cloos, 1992; Wang and Bilek, 2011). Wang and Bilek (2011) proposed a model to explain the seismogenic behavior of the subducting seamounts, based on the idea that the resistance is not always frictional when the seamount subducts. The behavior is controlled by the development of a complex network of fractures adjacent to the seamount that evolves with time during subduction. The complex structure and heterogeneous stresses of this fracture system provide a favorable condition for aseismic creep and small earthquakes, but not as favorable for the generation and propagation of large ruptures. For instance, the Maule (M_w 8.8) 2010 earthquake induced post-seismic afterslip at the upper portion of the megathrust north of the Maule earthquake rupture, which is bounded at the north by the San Antonio Canyon (~33.5°S), just south of the San Antonio seamount (Vigny et al., 2011; Lin et al., 2013). Also, inter-seismic coupling obtained from geodetic observations in Central Chile (Métois et al., 2012) indicates that San Antonio seamount is located in a transition zone between high and low coupling regions located at the northwestern and southeastern edges of the seamount, respectively. Thus, the southeastern and northwestern regions of the seamount being affected by high after-slip of the Maule earthquake and by the Valparaiso earthquake, respectively, is consistent with the propositions of Mochizuki et al. (2008) and Baba et al. (2001) for the stress behavior at the flanks of a subducting seamount.

The 2017 M_w 6.9 earthquake nucleated where the San Antonio seamount is currently subducting (Fig. 8a) propagating downdip for about 30 km. The same seismogenic zone has been broken several times by great earthquakes. The subducted San Antonio seamount, outlined in Fig. 8, has been inferred from the analysis of gravimetric anomalies, and its base has a diameter of approximately 30 km and its height is 3–4 km (Flores, 2007). From the moment tensor solutions, all the events analyzed (M ≥ 4.0) of the complete sequence occurred along the plate interface, correlating well at depth with Slab 1.0 (Hayes et al., 2012). The nucleation of the mainshock and the cluster of seismicity located over the current location of the seamount suggest an asperity-like behavior of the San Antonio seamount. Moreover, the narrow and complex slip distribution of the Valparaiso event, also suggest that the San Antonio seamount might have a higher topographic complexity (as seen for other non-subducted seamounts in the JFR) than the smooth one inferred by gravimetric methods. The same region has clustered seismicity. For instance, Lange et al. (2016) analyzed the aftershock seismicity associated to the 2015 M_w 8.3 Illapel earthquake and found a cluster located at the Topocalma Knoll (labeled C therein), which coincides with the location of the San Antonio subducting seamount. Along with the high seismic coupling and a subducting seamount at ~18 km depth, another possible explanation of the triggered seismicity is the intrusion of fluids and stress changes in the vicinity of the plate boundary that weakened the fault and initiated the precursory activity associated to the mainshock. The whole sequence probably was influenced by stress transfer of earthquakes and induced fluids flow.

6. Conclusions

We compute a detailed kinematic rupture model for the 2017 M_w

6.9 Valparaiso earthquake by joint inversion of teleseismic body waves and near-field datasets. The Akaike's Bayesian Information Criterion (ABIC) was used to treat both, (i) the problem of objectively estimating the relative weighting between datasets and (ii) to determine objectively the weighting of spatial and temporal constraints given as a priori information. Based on the work of Funning et al. (2014), we proved the feasibility of applying the ABIC criterion when combining teleseismic body waves and near-field datasets jointly. The coseismic slip is distributed over an area of dimensions $35 \times 10\,km^2$, extended mainly unilateral downdip, and with a peak-slip of 1.5 m. The source duration estimated from the moment-rate solution is ~20 s, with a total seismic moment of 3.05×10^{19} Nm (M_w 6.9). The seismic sequence occurred in April 2017 started two days before the mainshock, and lasted for about two weeks, and a migration of the seismicity was observed. The rupture of the 2017 M_w 6.9 earthquake nucleated where the San Antonio seamount is subducting, and propagated downward along a zone that presents high interseismic coupling. The nucleation of the mainshock and the seismicity clustered over and in the vicinity of the San Antonio seamount, located within a coupled zone, suggest an asperity-like behavior for the seamount. An aseismic slip transient in the surrounding zone next to the seamount, added to an heterogeneous asperity configuration, can explain the spatio-temporal complexity of the seismic sequence.

Acknowledgments

Regional moment tensors were computed using the mtpackagev1.1 package developed by Dr. Douglas Dreger of the Berkeley Seismological Laboratory, and Green's functions were computed using the FKRPROG software developed by Chandan Saikia of URS. Some figures were drawn using Generic Mapping Tools, v4.5 (Wessel and Smith, 1998). We thank comments provided by Dr. Pascal Bernard. This work was funded by the Chilean National Science Foundation through FONDECYT Project grant number 1170804. Eduardo Contreras-Reyes acknowledges the support of the Chilean National Science Foundation FONDECYT grant 1170009. We thank the support of Programa DE Investigación Asociativa: ANILLOS DE INVESTIGACION EN CIENCIA Y TECNOLOGÍA, CONICYT, grant ACT172002, project "The interplay between subduction processes and natural disasters in Chile". We are grateful to the Editor, and two anonymous reviewers for their constructive comments and suggestions, that helped us to improve the manuscript.

Appendix A. Supplementary data

Supplementary data associated with this article can be found, in the online version, at http://dx.doi.org/10.1016/j.pepi.2018.03.007.

References

Akaike, H., 1980. Likelihood and the Bayes procedure. In: Barnardo, J.M., DeGroot, M.H., Lindley, D.V., Smith, A.F.M., Valencia (Eds.), Bayesian Statistics. University Press, pp. 143–166.

Baba, T., Hori, T., Hirano, S., Cummins, P.R., Park, J.O., Kameyama, M., Kaneda, Y., 2001. Deformation of a seamount subducting beneath an accretionary prism: constraints from numerical simulation. Geophys. Res. Lett. 28, 1827–1830. http://dx.doi.org/10.1029/2000GL012266.

Bouchon, M., 1981. A simple method to calculate Green's functions for elastic layered media. Bull. Seism. Soc. Am. 71 (4), 959–971.

Cloos, M., 1992. Thrust-type subduction-zone earthquakes and seamount asperities: a physical model for seismic rupture. Geology 20, 601–604. http://dx.doi.org/10.1130/0091-7613(1992)020<0601:TTSZEA>2.3.CO;2.

Comte, D., Eisenberg, A., Lorca, E., Pardo, M., Ponce, L., Saragoni, R., Singh, S.K., Suarez, G., 1986. The 1985 central Chile Earthquake: a repeat of previous great earthquakes in the region? Science 233 (4762), 449–453. http://dx.doi.org/10.1126/science.233.4762.449.

Comte, D., Pardo, M., 1991. Reappraisal of great historical eathquakes in Northern Chile and Southern Peru seismic gaps. Nat. Hazards 4, 23–44.

Contreras-Reyes, E., Carrizo, D., 2011. Control of high oceanic features and subduction channel on earthquake ruptures along the Chile-Peru subduction zone. Phys. Earth Planet. Int. 186, 49–58. http://dx.doi.org/10.1016/j.pepi.2011.03.002.

Contreras-Reyes, E., Ruiz, J., Becerra, J., Kopp, H., Reichert, C., Maksymowicz, A., Arriagada, C., 2015. Structure and tectonics of the central Chilean margin (31°–33°S): implications for subduction erosion and shallow crustal seismicity. Geophys. J. Int. 653 (2), 776–791. http://dx.doi.org/10.1093/gji/ggv309.

Coutant, O. (1989). Programme de simulation numerique AXITRA, Tech. Report, LGIT, Grenoble, France.

Choy, G.L., Dewey, J.W., 1988. Rupture process of an extended earthquake sequence: teleseismic analysis of the Chilean Earthquake of March 3, 1985. J. Geophys. Res. 93 (B2), 1103–1118. http://dx.doi.org/10.1029/JB093iB02p01103.

Dreger, D.S., 2003. TDMT_INV: time domain seismic moment tensor inversion. Int. Handb. Earthq. Eng. Seismol. 81B, 1627.

Duputel, Z., Rivera, L., Kanamori, H., Hayes, G.P., 2012. W-phase fast source inversion for moderate to large earthquakes (1990–2010). Geophys. J. Int. 189 (2), 1125–1147.

Duputel, Z., Rivera, L., Kanamori, H., Hayes, G.P., Hirsorn, B., Weinstein, S., 2011. Real-time W phase inversions during the 2011 Tohoku-oki earthquake. Earth, Planets Space 63 (7), 535–539.

Flores, A., 2007. Caracterización de la Subducción de Montes Submarinos en el Márgen de Chile Central: Efectos Sobre el Campo de Esfuerzos (MSc Thesis). Universidad de Chile, Santiago, Chile.

Flueh, E.R., Vidal, N., Ranero, C.R., Hojka, A., von Huene, R., Bialas, J., Hinz, K., Cordoba, D., Danobeitia, J.J., Zelt, C., 1998. Seismic investigation of the continental margin off- and onshore Valparaiso, Chile. Tectonophysics 288, 251–263. http://dx.doi.org/10.1016/S0040-1951(97)00299-0.

Funning, G.J., Fukahata, Y., Yagi, Y., Parsons, B., 2014. A method for the joint inversion of geodetic and seismic waveform data using ABIC: application to the 1997 Manyi, Tibet, earthquake. Geophys. J. Int. 196, 1564–1579. http://dx.doi.org/10.1093/gji/ggt406.

Hayes, G.P., Wald, D.J., Johnson, R.L., 2012. Slab1.0: A three-dimensional model of global subduction zone geometries. J. Geophys. Res. 117, B01302. http://dx.doi.org/10.1029/2011JB008524.

Hayes, G.P., Rivera, L., Kanamori, H., 2009. Source inversion of the W-phase: realtime implementation and extension to low magnitudes. Seismol. Res. Lett. 80 (5), 817–822.

Ide, S., Takeo, M., 1997. Determination of constitutive relations of fault slip based on seismic wave analysis. J. Geophys. Res. 102 (B12), 27379–27391. http://dx.doi.org/10.1029/97JB02675.

Kanamori, H., 1993. W Phase. Geophys. Res. Lett. 20, 1691–1694. http://dx.doi.org/10.1029/93GL01883.

Kanamori, H., Rivera, L., 2008. Source inversion of W phase: Speeding up tsunami warning. Geophys. J. Int. 175, 222–238.

Kato, A., Fukuda, J., Kumazawa, T., Nakagawa, S., 2016. Accelerated nucleation of the 2014 Iquique, Chile Mw 8.2 Earthquake. Sci. Rep. 6, 1–9. http://dx.doi.org/10.1038/srep24792. 24792.

Kato, A., Obara, K., Igarashi, T., Tsuruoka, H., Nakagawa, S., Hirata, N., 2012. Propagation of slow slip leading up to the 2011 Mw 9.0 Tohoku-Oki earthquake. Science 335 (6069), 705–708. http://dx.doi.org/10.1126/science.1215141.

Khazaradze, G., Klotz, J., 2003. Short- and long-term effects of GPS measured crustal deformation rates along the south central Andes. J. Geophys. Res. 108, 2289. http://dx.doi.org/10.1029/2002JB001879.

Kikuchi, M., Kanamori, H., 1991. Inversion of complex body waves III. BSSA 81, 2335–2350.

Kodaira, S., Takahashi, N., Nakanishi, A., Miura, S., Kaneda, Y., 2000. Subducted seamount imaged in the rupture zone of the 1946 Nankaido earthquake. Science 289, 104–106. http://dx.doi.org/10.1126/science.289.5476.104.

Kopp, H., Flueh, E.R., Papenberg, C., Klaeschen, D., 2004. Seismic investigations of the O'Higgins Seamount Group and Juan Fernandez Ridge: aseismic ridge emplacement and lithosphere hydration. Tectonics 23http://dx.doi.org/10.1029/2003TC001590. TC2009.

Kubo, A., Fukuyama, E., Kawai, H., Nonomura, K., 2002. NIED seismic moment tensor catalogue for regional earthquakes around Japan: quality test and application. Tectonophysics 356 (1–3), 23–48. http://dx.doi.org/10.1016/S0040-1951(02)00375-X.

Lange, D., Geersen, J., Barrientos, S., Moreno, M., Grevemeyer, I., Contreras-Reyes, E., Kopp, H., 2016. Aftershock seismicity and tectonic setting of the 2015 September 16 Mw 8.3 Illapel earthquake, central Chile. Geophys. J. Int. 206 (2), 1424–1430. http://dx.doi.org/10.1093/gji/ggw218.

Laursen, J., Normark, W.R., 2002. Late Quaternary evolution of the San Antonio Submarine Canyon in the central Chile forearc (~33 S). Mar. Geol. 188 (3), 365–390.

Laursen, J., Scholl, D.W., von Huene, R., 2002. Neotectonic deformation of the central Chile margin: deepwater forearc basin formation in response to hot spot ridge and seamount subduction. Tectonics 21 (5), 1038. http://dx.doi.org/10.1029/2001TC901023.

Lawson, C.L., Hanson, R.J., 1974. Solving Least Squares Problems, Prentice-Hall Inc. Englewood Cliffs, New Jersey.

Lin, Y.N.N., Sladen, A., Ortega Culaciati, F., Simons, M., Avouac, J.-P., Fielding, E.J., Brooks, B.A., Bevis, M., Genrich, J., Rietbrock, A., Vigny, C., Smalley, R., Socquet, A., 2013. Coseismic and postseismic slip associated with the 2010 Maule Earthquake, Chile: characterizing the Arauco Peninsula barrier effect. J. Geophys. Res. Solid Earth 118 (6), 3142–3159. http://dx.doi.org/10.1002/jgrb.50207.

Lomnitz, C., 2004. Major earthquakes of Chile: a historical survey, 1535–1960. Seismol. Res. Lett. 75 (3), 368–378. http://dx.doi.org/10.1785/gssrl.75.3.368.

Malgrange, M., Deschamps, A., Madariaga, R., 1981. Thrust and extensional faulting under the Chilean coast: 1965 1971 Aconcagua earthquakes. Geophys. J. R. Astr. Soc. 66, 313–331.

Mendoza, C., Hartzell, S., Monfret, T., 1994. Wide-band analysis of the 3 March 1985

central Chile Earthquake – overall source process and rupture history. Bull. Seis. Soc. Am. 84 (2), 269–283.
Métois, M., Socquet, A., Vigny, C., 2012. Interseismic coupling, segmentation and mechanical behavior of the central Chile subduction zone. J. Geophys. Res. 117, B03406. http://dx.doi.org/10.1029/2011JB008736.
Mochizuki, K., Yamada, T., Shinohara, M., Yamanaka, Y., Kanazawa, T., 2008. Weak interplate coupling by seamounts and repeating M ~7 earthquakes. Science 321, 1194–1197. http://dx.doi.org/10.1126/science.1160250.
Moreno, M., Melnick, D., Rosenau, M., Baez, J., Klotz, J., Oncken, O., Tassara, A., Chen, J., Bataille, K., Bevis, M., 2012. Toward understanding tectonic control on the Mw 8.8 2010 Maule Chile earthquake. Earth Planet. Sci. Lett. 321, 152–165.
Nealy, J.L., Herman, M.W., Moore, G.L., Hayes, G.P., Benz, H.M., Bergman, E.A., Barrientos, S.E., 2017. 2017 Valparaíso earthquake sequence and the megathrust patchwork of central Chile. Geophys. Res. Lett. 44, 8865–8872. http://dx.doi.org/10.1002/2017GL074767.
Nishenko, S.P., 1985. Seismic potential for large and great interplate earthquakes along the Chilean and Southern Peruvian Margins of South America: a quantitative reappraisal. J. Geophys. Res. 90 (B5), 3589–3615. http://dx.doi.org/10.1029/JB090iB05p03589.
Pasyanos, M.E., Dreger, D.S., Romanowicz, B., 1996. Toward real-time estimation of regional moment tensors. Bull. Seism. Soc. Am. 86 (5), 1255–1269.
Roch, J., Duperray, P., Schindelé, F., 2016. Very fast characterization of focal mechanism parameters through w-phase centroid inversion in the context of tsunami warning. Pure Appl. Geophys. 173 (12), 3881–3893. http://dx.doi.org/10.1007/s00024-016-1258-3.
Ruiz, S., Aden-Antoniow, F., Baez, J.C., Otarola, C., Potin, B., del Campo, F., Poli, P., Flores, C., Satriano, C., Leyton, F., Madariaga, R., Bernard, P., 2017. Nucleation phase and dynamic inversion of the Mw 6.9 Valparaíso 2017 earthquake in Central Chile. Geophys. Res. Lett. 44, 10290–10297. http://dx.doi.org/10.1002/2017GL075675.
Ruiz, S., Klein, E., del Campo, F., Rivera, E., Poli, P., Métois, M., et al., 2016. The seismic sequence of the16 September 2015 Mw 8.3 Illapel, Chile, earthquake. Seismol. Res. Lett. 87, 789–799.
Ruiz, S., Metois, M., Fuenzalida, A., Ruiz, J., Leyton, F., Grandin, R., Vigny, C., Madariaga, R., Campos, J., 2014. Intense foreshocks and a slow slip event preceded the 2014 Iquique Mw 8.1 earthquake. Science 345 (6101), 1165–1169. http://dx.doi.org/10.1126/science.1256074.
Saikia, C.K., 1994. Modified frequency-wavenumber algorithm for regional seismograms using Filon's quadrature: modeling of Lg wave in eastern North America. Geophys. J. Int. 118, 142–158. http://dx.doi.org/10.1111/j.1365-246X.1994.tb04680.x.
Scholz, C.H., Small, C., 1997. The effect of seamount subduction on seismic coupling. Geology 25 (6), 487–490. http://dx.doi.org/10.1130/0091-7613(1997)025<0487:TEOSSO>2.3.CO;2.
Vigny, C., Socquet, A., Peyrat, S., Ruegg, J.C., Métois, M., Madariaga, R., Morvan, S., et al., 2011. The 2010 Mw 8.8 Maule Megathrust Earthquake of Central Chile, Monitored by GPS. Science 332 (6036), 1417–1421. http://dx.doi.org/10.1126/science.120413.
von Huene, R., Corvalán, J., Flueh, E.R., Hinz, K., Korstgard, J., Ranero, C.R., Weinrebe, E., 1997. Tectonic control of the subducting Juan Fernández Ridge on the Andean margin near Valparaiso. Chile, Tectonics 16 (3), 474–488.
Wang, K., Bilek, S.L., 2011. Do subducting seamounts generate or stop large earthquakes? Geology 39 (9), 819–822. http://dx.doi.org/10.1130/G31856.1.
Wessel, P., Smith, W.H.F., 1998. New, improved version of generic mapping tools released. EOS Trans. Amer. Geophys. Union 79 (47), 579.
Yáñez, G.A., Ranero, C.R., von Huene, R., Diaz, J., 2001. Magnetic anomaly interpretation across the southern central Andes (32°–34°S): the role of the Juan Fernández Ridge in the late Tertiary evolution of the margin. J. Geophys. Res. 106, 6325–6345.